A&A, 686, A23 (2024)
https://doi.org/10.1051/0004-6361/202347552

Astronomy & Astrophysics

CMEs evolve in the interplanetary medium to double their predicted geo-effectiveness

Shirsh Lata Soni[1,2], Anwesha Maharana[3], Antonio Guerrero[4], Wageesh Mishra[5], Stefaan Poedts[3,6], Smitha Thampi[2], and Mojtaba Akhavan-Tafti[1]

[1] Department of Climate and Space Science and Engineering (CLaSP), University of Michigan, Michigan 48105, USA
e-mail: shirshla@umich.edu
[2] Space Physics Laboratory, Vikram Sarabhai Space Center, Indian Space Research Organisation, Thiruvananthapuram 695022, India
[3] Centre for mathematical Plasma Astrophysics (CmPA), Dept. of Mathematics, KU Leuven, 3001 Leuven, Belgium
[4] Department of Physics and Mathematics, University of Alcala, Alcala, Spain
[5] Indian Institute of Astrophysics, Bengaluru 560034, India
[6] Institute of Physics, University of Maria Curie-Skłodowska, 20-031 Lublin, Poland

Received 24 July 2023 / Accepted 20 November 2023

ABSTRACT

Context. We explore the impact of interactions between coronal mass ejections (CMEs) – known as CME–CME interactions – on Earth using remote-sensing and in situ observations and estimate the amplification of the geo-effectiveness of the individual CMEs by a factor of ∼2 due to CME–CME interactions.
Aims. We present 3D reconstructions of interacting CMEs, which provide essential information on the orientation and interaction of the events. Additionally, we analysed coronal evolution of CMEs and their in situ characteristics at 1 AU to explore the impact of interactions between CMEs on their geo-effectiveness.
Methods. We analysed CME interaction using white light data from LASCO and STEREO COR-A. The reported CMEs were reconstructed using the gradual cylindrical shell (GCS) model and simulated self-consistently with the physics-based 3D MHD model EUHFORIA (EUropean Heliosphere FORecasting Information Asset). By running different simulations, we estimated the geo-effectiveness of both individual and interacting CMEs using an empirical relationship method for the disturbance storm index.
Results. The SOHO/LASCO spacecraft observed three CMEs erupting from the Sun within an interval of 10 h during a very active period in early November 2021. There were two partial halo CMEs that occurred on 1 Nov. 2021 at 19:00 UT and 22:00 UT, respectively, from the active region 12887 (S28W58), and a third halo CME occurred from AR 12891 (N17E03) on 2 Nov. 2021 at 02:48 UT. By combining remote observations close to the Sun, in situ data at 1 AU, and further numerical analyses of each individual CME, we are able to identify the initial and interplanetary evolution of the CMEs.
Conclusions. (i) White light observations and a 3D reconstruction of the CMEs show cannibalism by CME-2 on CME-1 and a flank interaction of CME-3 with the merged CME-1 and CME-2 at 45–50 Rs. (ii) Interacting CMEs exhibit an increase in geo-effectiveness compared to an individual CME.

Key words. Sun: corona – Sun: coronal mass ejections (CMEs) – Sun: evolution – solar-terrestrial relations

1. Introduction

Coronal mass ejections (CMEs) are the most dynamic expulsions of magnetised plasma structures from the Sun into the heliosphere. The interaction of two or more CMEs often occurs and depends on the propagation direction and speeds of the preceding and following CME(s). Such CME–CME interactions have long been recognised and studied using both remote and in situ observations of CMEs (Gopalswamy et al. 2001; Liu et al. 2012; Harrison et al. 2012; Temmer et al. 2014; Mishra et al. 2015). The propagation and plasma characteristics of a series of CMEs launched in quick succession are quite different from those of an individual CME propagating through the relatively quiet solar-wind background. This is because the preceding CMEs can substantially change the ambient solar-wind background and the following CMEs therefore travel through a preconditioned medium. Further, it is possible that CME–CME interactions lead to complex magnetic structures responsible for strong geomagnetic storms (Farrugia et al. 2006; Lugaz & Farrugia 2014; Scolini et al. 2020; Koehn et al. 2022; Maharana et al. 2023). The probability of CME interactions or the shocks they drive is comparatively high during the maximum phase of the solar cycle when even a single active region produces multiple CMEs within a few hours (Yashiro et al. 2004). However, the possibility of CME–CME interaction during the rising and declining phases of a solar cycle, although comparatively low, cannot be ignored.

Before observational data from the Solar TErrestrial RElations Observatory (STEREO) Kaiser et al. (2008) became available, only a handful cases of interacting CMEs had been discovered in white-light observations of the corona. However, since the STEREO era, several authors have analysed interacting CMEs (Scolini et al. 2020; Joshi et al. 2018; Temmer et al. 2014, and references therein). This is because the heliospheric imagers (HIs) on board STEREO were able to observe the vast and crucial distance between the Sun and Earth, enabling observation of CME–CME interactions at different heliocentric distances from the Sun (Möstl et al. 2012; Temmer et al. 2014;

Mishra et al. 2017). Several studies have investigated the interacting CMEs to understand the evolution of the shock strength, structure, and its effect on the plasma parameters of the preceding CME(s) (Möstl et al. 2012; Liu et al. 2012; Mishra et al. 2015). The orientation and shape of the magnetic flux rope within a CME is widely acknowledged as having a significant impact on its subsequent evolution and propagation in the interplanetary space (Lugaz et al. 2005, 2013). A series of studies tracking CMEs in the heliosphere and estimating their 3D kinematics have attempted to understand the nature of CME–CME interactions and/or collisions (Shen et al. 2012; Mishra et al. 2016; Koehn et al. 2022). These studies have shown that the interacting CMEs undergo changes in their kinematics and morphology during the interaction. Therefore, the prediction of their arrival time to Earth using preinteraction kinematics may lead to a larger error on estimations of their arrival time. Furthermore, most of the CME–CME interaction studies reported in the literature are based on CMEs originating from the same active region on the Sun. Therefore, it would be interesting to also study the behaviour of interacting CMEs originating from different source regions and to examine the signature of such interactions with both white-light observations and numerical simulations.

In the present work, we studied the interaction and geo-effectiveness of three consecutive CMEs that erupted in a time window of around 10 h on 1 and 2 November 2021 from two different active regions. We monitor the structures of all three CMEs using coronagraph and heliospheric imager observations. We obtained a 3D reconstruction of the CMEs in order to estimate their deprojected speeds and their direction of propagation. Our analysis allows us to better comprehend the coronal evolution and interplanetary traces of the selected CMEs. Our analysis, using running-difference images, establishes a definite shock signature ahead of the CME eruption. In Sect. 2, we describe the data sources and the detailed characteristics of the reported CME events from their source location to their interplanetary trajectories. In Sect. 3, we present numerical simulations to model the successively interacting CMEs using the linear force-free spheromak CME model in the framework of the 3D magnetohydrodynamic (MHD) model EUHFORIA (Pomoell & Poedts 2018). We explore CME–CME interactions for a range of orientations, launch-time variations, and CME handedness and quantify their geo-effectiveness via the primary solar-wind variables and empirical measures of the disturbance storm time index and subsolar magnetopause stand-off distance. We explore the role of CME–CME interaction in creating extreme geo-effective conditions. In Sect. 4, we analyse the geo-effectiveness of the interaction using a prediction of the disturbance on the ground as indicated by the SYM-H index and Sect. 5 provides a summary of this study.

2. Observations and analysis

For the analysis of the selected CMEs and the associated solar flares, we used observational data from GOES X-ray flux and EUV observations from the Atmospheric Imaging Assembly (AIA) on board the Solar Dynamics Observatory (SDO; Lemen et al. 2011). We also use white-light coronagraphic observations from the Sun–Earth Connection Coronal and Heliospheric Investigation (SECCHI) suite on board STEREO and LASCO-C2/C3 on board SOlar and Heliospheric Observatory (SOHO) (Domingo et al. 1995; Brueckner et al. 1995), the locations of the spacecraft are shown in Fig. 1[1].

[1] https://stereo-ssc.nascom.nasa.gov/cgi-bin/make_where_gif

We note that on November 2, 2021, GOES detected a long-duration X-ray multiple events of flare class C1.0, C5.3, and M1.3 Fig. 2[2]. These flares started at heliographic coordinates S27W76 and N17E03 from two active regions 12887 and 12891, respectively. To identify the two-dimensional orientation of CME propagation, we used white-light observations processed by segmentation and CACtus techniques and available at Space weather web-pages[3,4]. We implemented the graduated cylindrical shell (GCS) model (Thernisien 2011) to reconstruct the 3D trajectory of CME events. We used the co-temporal observations of CMEs from multiple viewpoints (STEREO and SOHO) and estimated the true heights of the CMEs.

Our observations suggest that the active regions NOAA 12887, located close to the southwest limb (S27W76), and NOAA 12891, located at N17E03 were highly eruptive in early November 2021. Multi-step flares were observed from 17:00 UT (1 Nov. 2021) to 08:00 UT (2 Nov. 2021) from the X-ray Sensor (XRS[5]) on board the GOES spacecraft. Figure 2a displays the GOES X-ray flux profiles of the flare events during this period in the 1−8 Å and 0.5−4 Å wavelength bands. The fluxes in these channels started to rise at 17:00 UT on 1 Nov. 2021 and reached a first peak (C0.5) within about 30 min and started decaying. Again, at ∼21:00 UT on 1 Nov. 2021, the flux started rising and peaked for a second time (C 3.1) and returned to the background value after about two hours. At 01:30 UT on 2 Nov. 2021, flux started increasing again and reached a further peak at 02:40 UT on 2 Nov. 2021; after a long decay phase the flux then merged with the background at around 08:00 UT. It is also to be noted that the hard X-ray flux (0.5−4 Å) increased by more than about two orders of magnitude in comparison with its mean background value. However, the soft X-ray (1−8 Å) spectrum increased by only about one order with respect to its background. It is likely that the heating at the flare site was sufficient to produce the hard part of the X-ray spectrum.

We further analysed the solar-wind observations from the Wind spacecraft located at L1. We find signatures of the arrival of an interplanetary CME (ICME) at L1 approximately 16 h after the occurrence of CME events on the Sun. The identified ICME is found to have a strong southward interplanetary magnetic field. The identified ICME resulted in a sudden storm and gave rise to the first most intense geomagnetic storm of sunspot cycle 25, with a Dst index of −115 nT at November 3, 2021 on 21:10 UT. Also, the arrival of an ICME lead to aurora in northern high-to-middle latitudes over three days from November 2-4, 2021 and also lead to a significant drop in cosmic-ray fluxes on the ground[6]. These geomagnetic activities associated with the identified ICME are one of the major space weather events of solar cycle 25.

The location of the STEREO-A spacecraft around the launch of the CMEs was 37° away from Earth and provided a good view of the selected Earth-directed CMEs in the corona. Based on the running difference images obtained from SOHO and STEREO coronagraphs, it is possible that three CMEs launched from the Sun in quick succession and interacted close to the Sun itself in the coronagraphic field of view. We used coronagraphic observations of CMEs from multiple viewpoints from SOHO and STEREO for the 3D reconstruction of the CMEs. The overlapping field of view of the coronagraphs on STEREO and SOHO

[2] https://www.polarlicht-vorhersage.de/goes-archive
[3] http://spaceweather.gmu.edu
[4] https://www.sidc.be/cactus/
[5] www.ssec.wisc.edu
[6] https://earthsky.org/sun/aurora-alert-nov-2021-halo

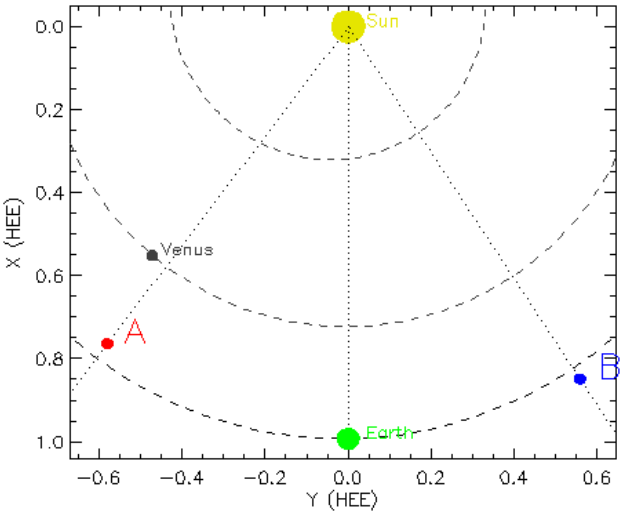

Fig. 1. Location of spacecraft used for observations in the heliosphere, where A and B are STEREO-A and STEREO-B respectively.

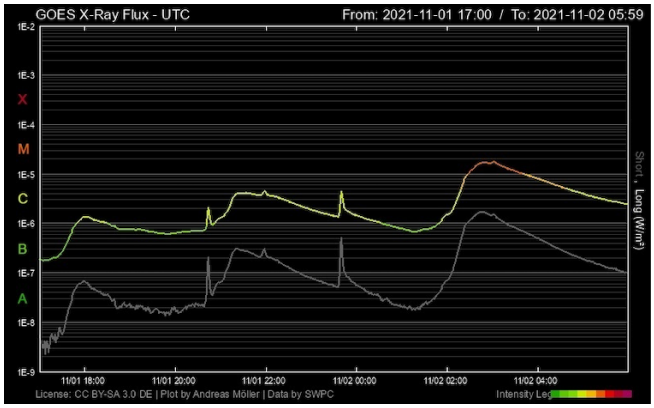

Fig. 2. GOES X-ray plot for solar flare occurred on 1 Nov. 2021, 17:00 UT. In this plot, the coloured curve shows the flux emission for energy bands 1–8 Å and the grey curve the flux emission for the 0.25–4 Å band.

enables us to derive the 3D properties of the CMEs. The source location of the CME on the Sun (back-projecting the CME apex along a straight line normal to the solar surface), the direction of propagation, the edge-on and face-on width of the CME, and the propagation speed are all determined from the GCS model of the 3D reconstruction. The GCS model (Thernisien 2011) can fit the geometry of the CMEs by varying their 3D trajectories. Therefore, we can derive the best-fit 3D parameters of the CMEs, which can reproduce the CMEs observed in the coronagraphic images from different viewpoints.

The trajectories, orientations, velocities, and source regions of the CMEs are inferred from the GCS model-fit parameters. Further, we examined the extreme-ultraviolet (EUV) observations from the SDO/AIA to confirm the source regions. The source region of CME-1, CME-2, and CME-3 was visible in all coronal wavelength filters of SDO/AIA. The 171 Å images from AIA/SDO revealed a flux-rope eruption associated with CMEs. Because of the great temporal and spacial resolution of AIA, we can see the independent eruptions at the source regions that led to the commencement of these three CMEs. We can determine the orientation of propagating CMEs using two separate vantage points from which they are observed. Further details about the three selected CMEs are discussed below.

2.1. CME-1

The first CME (CME-1) was associated with a C1.0 class flare eruption as measured by GOES on 1 November, 2021 (Fig. 2). CME-1 appears in the southeast quadrant of the STEREO/COR2 and LASCO-C2 field of view on 1 November, 2021, at 18:36 UT. The faint flux-rope-like structure was observed by the SDO/AIA 171 Å filter at 18:38 UT on 1 November, 2021, and can be seen in the top panel of Figs. 3a,b. The upper transition area of the solar atmosphere is covered by this wavelength band. The 2D appearance of CME-1 using the segmentation technique and CACtus, the Figs. 3c,d (directly taken from Space weather webpage[7]) shows that CME-1 was directed southwest and it is 70° wide at the height of 5.9 Rs on 20:12 UT (taken from CACtus[8]). The GCS model fits (blue) overlaid on the observed running-difference images of the STEREO-A COR2 and LASCO/SOHO C2 coronagraphs at 20:23 UT on 1 November, 2021, are shown in the bottom panels of Figs. 3e,f.

From the 3D reconstruction of CME-1, we find that it is propagating in the direction of S28W58 (southwest of the Sun–Earth line) when the leading edge of the CME is at 8.3 $R_\odot$. We were able to unambiguously track the CME and fitted it using the GCS model from its first appearance in COR2 until its exit from the COR2 field of view. From the derived fitted parameters from the GCS model, we obtain the 3D kinematics of CME-1, which is reported in Table 1. Our estimates of the height–time measurements show that the average propagation speed of CME-1 is around 545 km s^{-1}. The propagation direction of CME-1 around 30° away from the Sun–Earth line suggests that the flank of the CME might reach the Earth. However, assuming the CME speed measured in the coronagraphic field of view to be constant throughout its interplanetary journey, we could not identify any ICME in the in situ observations at L1, which can be associated with CME-1. As discussed above, there are other CMEs following CME-1; it is possible that CME–CME interactions took place, which we investigated by analysing the observations of the following CMEs, as detailed below.

2.2. CME-2

The second CME (CME-2) appeared in the STEREO COR2 observations at 21:38 UT on November 1, 2021. The eruption of CME-2 was accompanied by a minor flare. The soft X-ray emission rose at 21:00 UT, reaching approximately C5.3 class levels by 21:30 UT according to GOES measurements. During this time, the AIA 171 Å observations reveal flaring within the active region across a limited portion of the active region. Around the emergence of CME-2, the CME-1 leading edge reached around 10 $R_\odot$. The source region of CME-2 is NOAA AR 12887, which is located at S28W58. Figure 4 shows the observations of CME-2 from the STEREO-A COR2 and LASCO/SOHO C3 coronagraphs at the height of 13.31 $R_\odot$ at 23:42 UT on November 1, 2021. In SDO/AIA 171 Å observations, the source of CME-2, AR 12887, is shown in Figs. 4a,b, the vibrant and fainter loops detected rising higher, which were also linked to CME-1. The loops that erupt later with CME-2 are present in the source region before and after the eruption of CME-1, indicating that this is merely a partial eruption of the active region. In AIA

[7] http://spaceweather.gmu.edu
[8] https://www.sidc.be/cactus/

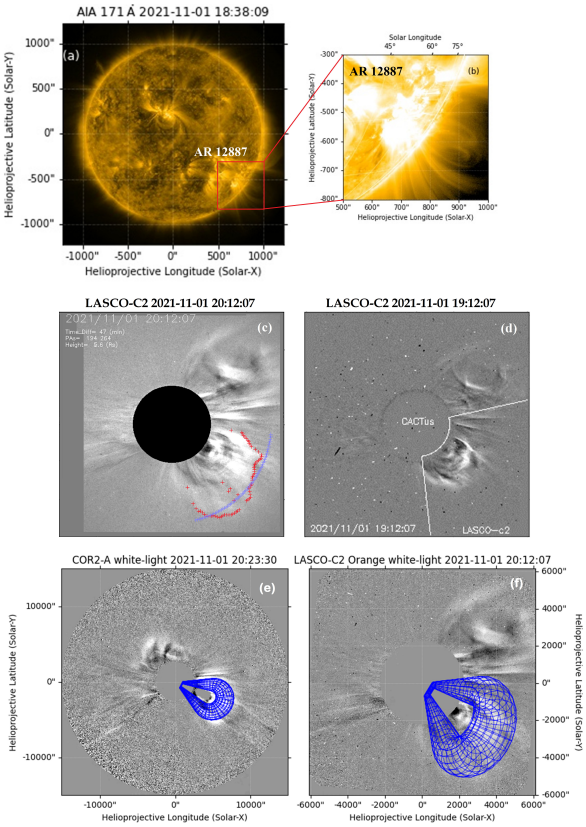

Fig. 3. Observations associated with CME-1. (a) SDO/AIA 171 Å filter image of source active region of CME-1 on 01 Nov. 2021 18:38 UT, and zoom snap of AR 12887, showing the flux rope orientation of source region. (c) Running-difference C2 images, the blue color indicates the boundary of the leading edge of CME and red color on the difference image shows an position of leading edge (approximated) obtained using segmentation technique. (d) Running difference images of C2 indicates the direction and width of CME using CACtus. (e) and (f) Corresponding GCS modeling (blue grids) from STEREO-A and LASCO respectively, detectors and times are given in the images.

171 Å observations, the CME-2 erupting loops appear to have a southwest orientation that is roughly perpendicular to the magnetic dipole orientation of the active region. These loops are oriented similarly to the GCS model, as seen in Figs. 4e,f.

We employed the GCS model of 3D reconstruction and determined the various 3D parameters of CME-2. The GCS fits of CME-2 are shown in Figs. 4e,f. The initial speed of CME-2 is around 829 km s^{-1} which is substantially faster than CME-1. CME-2 has a longitude of 16° and a latitude of 48°. The propagation direction of CME-2 suggests that it is propagating in almost the same direction as CME-1. We also noticed that the tilt angles of CMEs are approximately identical (64.53° and 62.83°, respectively), consistent with the orientations of their respective source regions. Further, the CME-2 has a higher speed and angular width than the CME-1 and therefore it is possible that CME-2 might have caught up with CME-1. Moreover, the plane-of-sky projected observations from LASCO suggest that both CMEs (CME-1 and CME-2) are possibly interacting at around 22 $R_\odot$ (Fig. 4), which is further confirmed by simulations (Sect. 3.3).

2.3. CME-3

The third CME (CME-3) was identified as a halo CME from both SOHO/LASCO and SECCHI COR2 perspectives. CME-3 enters the STEREO-A COR2 field of view at 02:48 UT on November 2, 2021. Its eruption is accompanied by an M 1.3 X-ray flare from AR 12891. CME-3 has a broad front and emerges swiftly at a plane-of-sky speed of 1335 km s^{-1} in the LASCO/SOHO C2 observations (GCS: 1384 km s^{-1}). The CME is seen edge-on from the STEREO-A COR2 viewpoint and has a narrower breadth than seen from the LASCO/SOHO viewpoints. CME-3 was low in the corona at roughly 03:23 UT on November 2, 2021, as seen in Figs. 5c,d. CME-3 is found to originate from the source region at N27E58 and is associated with an M 1.3 flare, with a peak at 02:40 UT and a slow drop over 2 h. As seen in Figs. 5a,b, the loops that erupt with CME-3 were present in the source active region for several hours before, during, and after the eruption of CME-3. Figure 5b depicts the CME-3 eruption loops in a relatively stable form at 02:40 UT. A twisted structure may be seen erupting in all of the AIA coronal wavelengths around 02:40 UT. This structure is visible in 171 Å data, indicating the presence of a hot flux rope structure (Fig. 5b). The loops of CME-3 appear to be oriented approximately north-west with the magnetic polarity of the active zone based on AIA measurements.

As CME-3 develops in the white-light coronagraphic field of view, a bright structure forms on the northeast limb of the STEREO-A COR2 image (Fig. 5c). In the LASCO C2 image, a similar structure can be seen on the northeast limb (Fig. 5d). We identify this structure as a shock driven by CME-3. The evidence of the shock candidate caused by CME-3 can also be observed in the sequence of coronagraphic images from SOHO/LASCO at L1 (Fig. 5a). The driven shock becomes more visible as CME-3 moves further outward in the corona. We utilized the GCS model on the simultaneous images of CME-3 captured from SOHO/LASCO and STEREO/COR viewpoints, with the GCS fitted wire-frame overlaid on the CME images, as depicted in Figs. 5e,f. The propagation direction of CME-3 is along the Sun–Earth line, which suggests its arrival at the Earth. Further, the speed of CME-3 is much greater than that of both the preceding CMEs (CME-1 and CME-2). Therefore, it is possible that CME-3 may interact with the flank of CME-1 and/or CME-2 depending on the kinematics of the CMEs beyond the coronagraphic field of view. As the CME-driven shock is of larger angular width than the driving CME, it is also possible that a CME3-driven shock would interact with preceding CMEs. We examine these possibilities in the following sections.

2.4. CME–CME interaction in white-light observations

As described earlier, two active locations, NOAA 12887 and NOAA 12891, show strong flaring activity and eruptions on November 1 and 2, 2021. The observations establish the launch of two CMEs (CME-1 and CME-2) in quick succession from the same active region NOAA 12887. The first appearance of CME-1 is shown in Fig. 6a, which occurred at 18:38 UT on November 1, 2021, with a speed of 545 km s^{-1} in the field of view of the LASCO/SOHO C2 coronagraph. The STEREO-A COR2 coronagraph first identified CME-2 at a height of 2.6 $R_\odot$ at 21:36 UT on November 1, 2021. We also identified a shock driven by CME-2, which has a speed of 829 km s^{-1}. The speeds of CMEs are corrected for the plane-of-sky projection effect obtained from GCS fittings. The CME-2 overtakes the preceding slower CME-1 as seen in Fig. 6b. The merging of CME-1 and CME-2 could be followed up to a height of around 21 $R_\odot$, as seen in Fig. 6c. We estimate that the velocity of the merged CMEs (CME-1+CME-2) increased by 4%. The degree of error observed is not unique to the methodology employed in this

Table 1. Parameters obtained from Triple-spacecraft GCS Fits of the CME-1 and CME-2.

Events	Date and time	Source region	Flare (class)	ϕ(°)	θ(°)	H ($R_\odot$)	w (°)	k	γ (°)
CME-1	01/11/2021 18:36 UT	AR12887 (S28W58)	C 1.0	30	−27	8.3	29	0.2	64
CME-2	01/11/2021 21:48 UT	AR12887 (S28W58)	C 5.3	48.4	−16.9	13.3	48.2	0.2	63
CME-3	02/11/2021 02:48 UT	AR12891 (N17E03)	M 1.3	−1	23.7	9.6	45	0.5	−56

Notes. Longitude: θ (degree) and latitude: ϕ (degree), tilt angle: γ (degree), CME height: H ($R_\odot$), aspect ratio: k, and half-angle: w (degree).

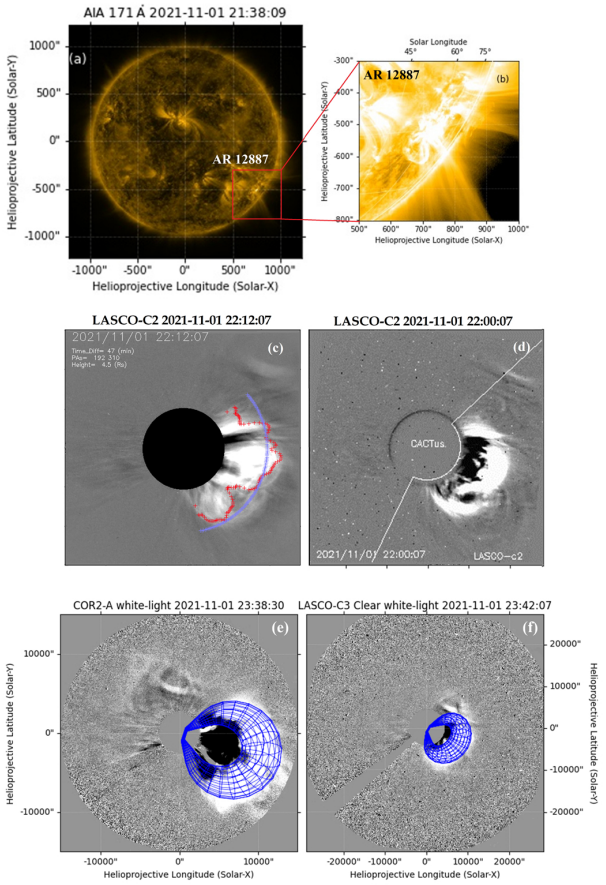

Fig. 4. Observations associated with CME-2. (a) The source active region AR 12887 in EUV image of 171 Å filter obtained from AIA/SDO on 21:38 UT at 01 Nov. 2021. (b) Zoomed in cutout of source active region of CME-2. (c) and (d) The running difference images obtained from LASCO presenting the orientation of CMEs in 2D (source and description of (c) is as mentioned in Fig. 1). And corresponding GCS fit in (e) and (f) for STEREO-A/ COR-A and LASCO/SOHO C3 coronagraph respectively.

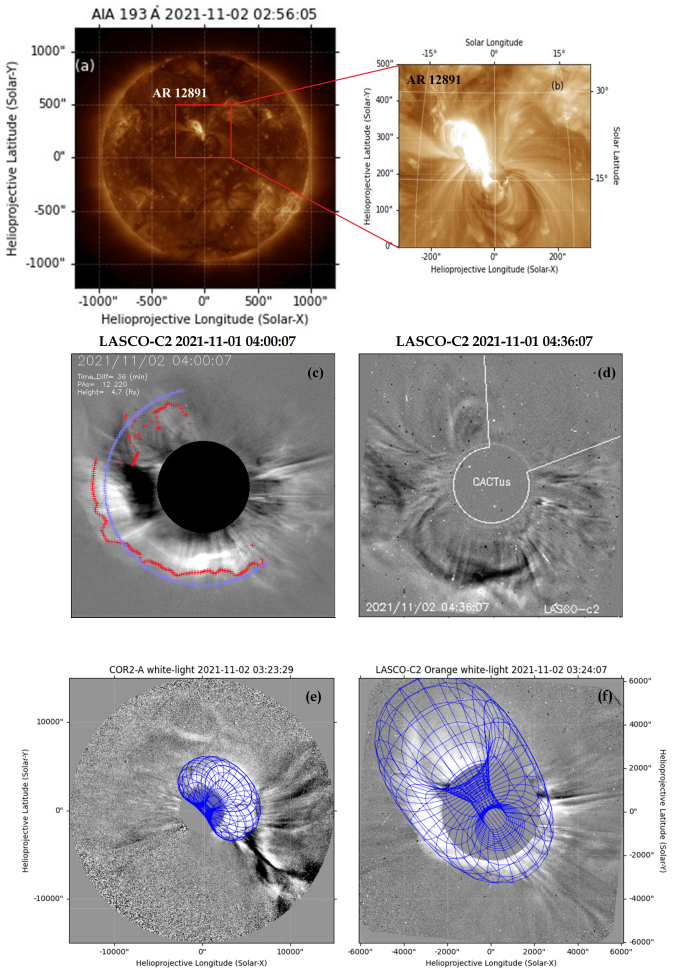

Fig. 5. Observations associated with CME-3. (a) EUV images at 193 Å of source active region observed from SDO. (b) EUV images at 02:56 UT on 02 Nov. 2021 showing the flux rope direction and eruption from active region 12891. (c) and (d) Running difference images from LASCO/SOHO C2 corona graph highlighting the propagation of CME in heliosphere in 2D using segmentation technique and CACtus software (source and description of (c) are as mentioned in Fig. 1). Contemporaneous observations of CME-3 from STEREO-A COR2 and LASCO C2 and the GCS fit (blue) over plotted for each viewpoint.

study; instead, it is prevalent in similar cases. We observed CME-3 within the 5 h following CME-2. Due to the higher speed of CME-3, which is propagating along the Sun–Earth line, we expect that it was able to catch up with the preceding merged structures formed due to the interaction of CME-1 with CME-2.

We estimated the height–time data obtained from the GCS model for 3D reconstructions of CMEs. The estimated true heights of the three selected CMEs are shown in Fig. 6e. In the figure, the CME-1 heights are shown with green squares, the CME-2 heights with red circles, and the CME-3 heights are indicated with blue triangles. The height–time profile of the CMEs confirms the notion of interaction of the CMEs in the corona and interplanetary space. To explore the interactions between the selected CMEs in more detail, we followed the CME trajectories observed by the imaging suite on board STEREO-A. The imaging package of this spacecraft includes five telescopes, an Extreme Ultra Violet Imager (EUVI), two white-light coronagraphs (COR1 and COR2), and two white-light heliospheric imagers (HI1 and HI2) (Howard et al. 2008). To track the evolution of the CMEs in the heliosphere, we examined the observations from COR2 (2.5–15 $R_\odot$) and heliospheric imagers (HI-1: 15–84 $R_\odot$ and HI-2: 66–318 $R_\odot$) (Fig. 6).

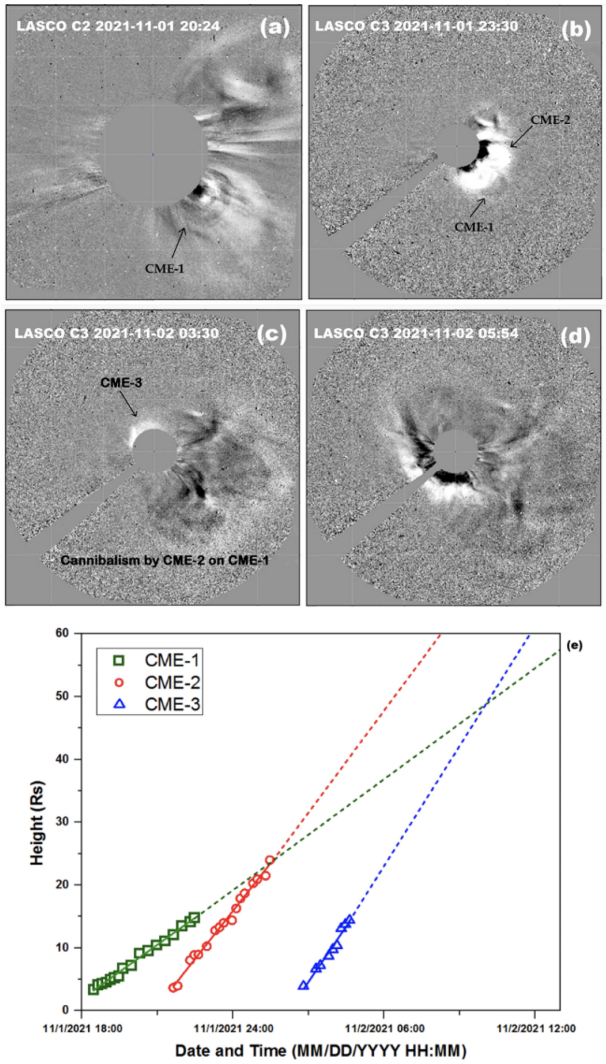

Fig. 6. Presentation of CME–CME interaction based on white-light observations from LASCO/SOHO viewpoint.

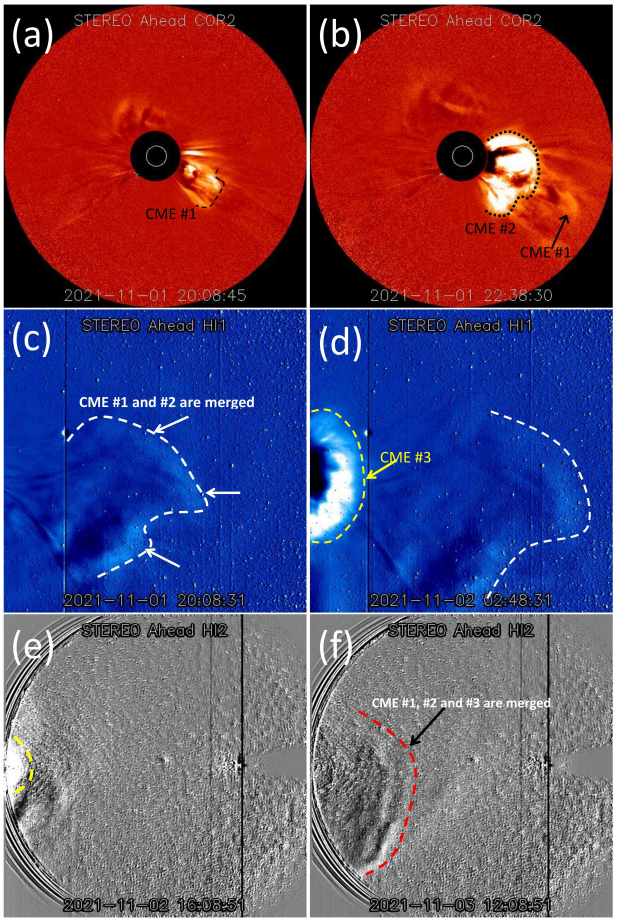

Fig. 7. Presentation of CME–CME interaction based on white-light observations from STEREO viewpoint.

The SECCHI suite imaging the vast distance between the Sun and Earth enables us to infer the trajectory of the selected CMEs. In our analysis, the direction and propagation speed of the apex of the CME front (i.e. CME front farthest from the Sun) are referred to as the 'CME trajectory'. Further, we examined the in situ observations of large-scale solar-wind structures arriving at L1 in order to confirm the scenario of CME–CME interaction for the selected CMEs.

Figure 7a shows the leading edge of CME-1 (marked by the black dash curve on 1 Nov. 2021 at 20:08 UT) and Fig. 7b at 22:38 UT shows the following CME, CME-2, interacting with the trailing edge remnants of CME-1. The signatures of CME-1 and CME-2 can be clearly traced in the STEREO-A/COR2 field of view. The interaction of these two CMEs can also be easily seen in the HI1 field of view as shown in Fig. 7c. In the observed image of HI1 on 2 Nov. 2022 at 02:48 UT, we can see the merged structure of CME-1 and CME-2 at ~60–80 $R_\odot$. Figure 7d also shows the appearance of CME-3 at the entrance of the HI1 field of view at ~25 Rs. Figures 7e,f show the HI2 observations where we can see the merged structure of CME-3 with the earlier merged CME-1 and CME-2. This finding of an interaction scenario is consistent with the heights estimated for the selected CMEs. We derive that CME-1 and CME-2 interact at a height of 22 $R_\odot$, and their merged ejecta (CME-1+CME-2, hereafter) also interact with CME-3 at a height of ~46 $R_\odot$.

The estimated true height of the CME–CME interaction may slightly vary depending on the reconstruction method used to estimate the heliocentric distances of the leading edges of CMEs. The performances of different reconstruction methods for estimating the CME kinematics were examined by Mishra et al. (2014). A more comprehensive analysis of CME–CME interaction could have been done by deriving the time-elongation profile of the tracked CMEs and using that in the stereoscopic self-similar expansion (SSSE) method as done in earlier studies (Mishra & Srivastava 2014; Mishra et al. 2017; Scolini et al. 2020; Palmerio et al. 2021). However, implementing the SSSE method on the HI observations from STEREO is no longer possible, as STEREO-B was lost in 2014, and therefore HI observations for the selected CMEs are only available from STEREO-A. There are only a few case studies reported in the literature confirming the CME–CME interaction of three participating CMEs. Therefore, we approach this case of CME–CME interaction with numerical MHD simulations.

3. Numerical modelling of the event with EUHFORIA

In this section, we perform MHD simulations to model the propagation of the CMEs in the heliosphere beyond 21.5 $R_\odot$ (0.1 AU). We present the simulation setup of the ambient solar wind and the CMEs in the framework of the physics-based space-weather

forecasting model called EUropean Heliospheric FORecasting Information Asset (EUHFORIA; Pomoell & Poedts 2018). The question that we seek to answer is how the magnetic ejecta formed due to the interaction between CME-1 and CME-2 affects the propagation and magnetic field signature of CME-3.

3.1. EUHFORIA setup

EUHFORIA constitutes a combination of a (simple) coronal model and a MHD heliospheric model (version 2.0). The coronal model used for this work is a 3D semi-empirical model, which is a modified version of the model presented by Wang-Sheeley-Arge Sheeley (2017). This model, driven by photospheric magnetic field observations, computes the plasma and magnetic field conditions at 0.1 AU (which is the inner boundary of the EUHFORIA heliospheric model). The output of the coronal model serves as the boundary condition for the heliospheric model, which numerically solves the ideal MHD equations in 3D. The resolution of the computational mesh is 0.0037 AU (corresponding to 0.798 Rs) with 512 equidistant cells in the radial direction (from 0.1 AU to 2 AU), and the angular resolution is 4° in the latitudinal (extending between ±80°) and 2° in the longitudinal (extending between 0−360°) directions, respectively.

3.2. Background solar-wind modelling

In a EUHFORIA simulation, the background solar wind before the CME onset is first modelled to ensure appropriate plasma and magnetic field conditions in which the CMEs traverse. The synoptic magnetogram from the Global Oscillation Network Group - Data Assimilative Photospheric Flux Transport (GONG-ADAPT) provider from October 31, 2021 at 12:04 UT (mrbqs211031t1204c2250_173.fits.gz) was selected to model the solar wind as it corresponds to the time before the eruption of all the CMEs. In situ observations suggest the presence of a high-speed stream before the arrival of the CMEs. We need an appropriate and realistic solar-wind background to ensure accurate modelling of the CMEs. We therefore optimise the fitting of the simulated wind to observations by rotating the magnetogram by one day to adjust the arrival time of the high-speed stream at Earth.

3.3. CME modelling

CMEs are injected as time-dependent boundary conditions at the inner boundary of the EUHFORIA heliospheric model (0.1 AU). We employ the linear force-free magnetised spheromak model (Chandrasekhar & Woltjer 1958) implemented in EUHFORIA (Verbeke et al. 2019) for modelling the CMEs of this event. The initial conditions needed to run the spheromak model are constrained by the observed geometrical and magnetic field properties of the CMEs. The spheromak model requires the following geometrical parameters: injection time at 0.1 AU, latitude (θ), longitude (ϕ), radius (R), radial speed ($v_{\rm rad}$); the plasma parameters: mass density ($\rho_{\rm CME}$) and temperature ($T_{\rm CME}$); and the magnetic field parameters: the sign of the helicity (H), tilt (γ), and toroidal flux (ϕ_t). The geometrical parameters are obtained from the GCS reconstruction of the CMEs below 0.1 AU as given in Table 1. The poloidal magnetic flux (reconnection flux) is obtained by averaging the values obtained by Kazachenko et al. (2017), Dissauer et al. (2018), and Tschernitz et al. (2018) using the flare peak intensity in soft-X-ray. The poloidal flux is then converted into toroidal flux using the following computation,

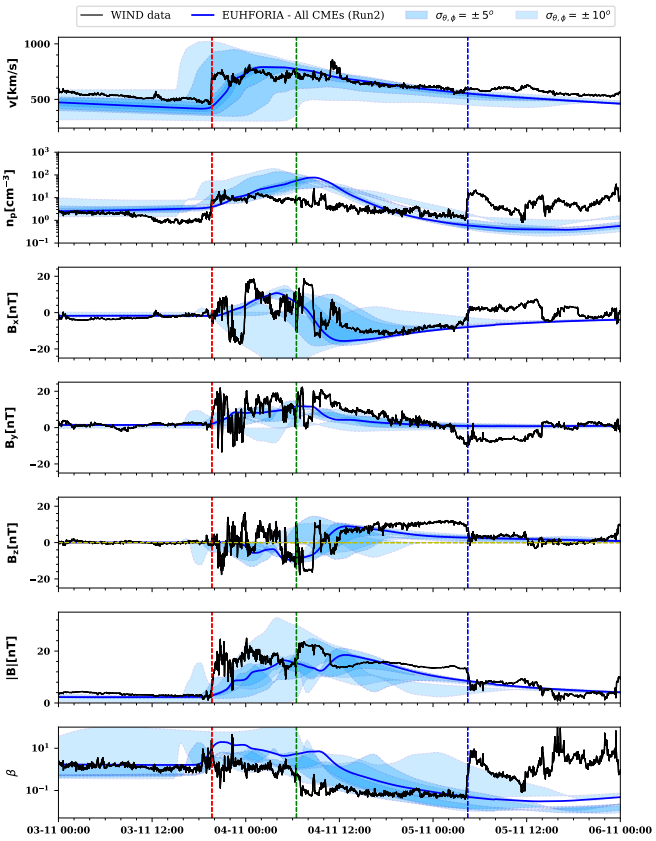

Fig. 8. Time series plot showing the comparison between the simulations with CME-1, CME-2 and CME-3 modelled with the spheromak model at Earth (in blue).

which is presented in Scolini et al. (2019). The CME temperature is set to the standard 0.8 MK following Pomoell & Poedts (2018). The CME density is set to 5×10^{-18} kg m^{-3}, which is five-fold higher than the standard 1×10^{-18} kg m^{-3} proposed by Pomoell & Poedts (2018). The enhancement in density is considered to mitigate the effect of spheromak tilting instability, which could result in erroneous space-weather predictions (Asvestari et al. 2022).

We performed two EUHFORIA simulations: Run1 involves simulating the evolution of only CME-3 and Run2 is a self-consistent simulation of CME-1, CME-2, and CME-3. Run1 serves as a proxy to understand the effect of CME–CME interaction on the plasma and magnetic field properties of CME-3 at Earth in the presence of CME-1 and CME-2.

3.4. CME arrival at Earth

The simulation results are consistent with the propagation suggested by the close-to-Sun white-light image reconstruction as discussed in Sect. 2.4. The bulk of CME-3 travels almost along the Sun–Earth line and towards the north of the ecliptic, and contributes the most to the impact on Earth. CME-1 and CME-2 are propagating in the southwest direction from the Sun–Earth line. We analysed the impact of the presence of CME-1 and CME-2 in front of CME-3 by comparing Run1 and Run2. The temporal evolution of the speed, magnetic field components, and the plasma beta (β) for Run2 at Earth can be found in Fig. 8. The shaded regions correspond to the plasma and magnetic field properties at virtual satellites placed at ±5°

Table 2. Initial parameters used to inject CMEs at 0.1 AU (EUHFORIA heliospheric domain) in the simulations using the LFF spheromak model.

CME	Injection time	θ	ϕ	R	$v_{\rm rad}$	$\rho_{\rm CME}$	$T_{\rm CME}$	H	γ	ϕ_t
CME-1	2021-11-01 23:17:00 UT	−27	30	14	454	$5 \cdot 10^{-18}$	$8 \cdot 10^{5}$	+1	−45	$0.9 \cdot 10^{13}$
CME-2	2021-11-02 00:58:00 UT	−17	48	19	691	$5 \cdot 10^{-18}$	$8 \cdot 10^{5}$	+1	−45	$1.3 \cdot 10^{13}$
CME-3	2021-11-02 05:08:00 UT	24	−1	21	890	$5 \cdot 10^{-18}$	$8 \cdot 10^{5}$	−1	−100	$3 \cdot 10^{13}$

Notes. Injection time (yyyy-mm-dd HH:MM:SS in UT), latitude: θ (°), longitude: ϕ (°), radius: R ($R_\odot$), radial speed: $v_{\rm rad}$ (km s^{-1}), density: $\rho_{\rm CME}$, temperature: $T_{\rm CME}$ (K), chirality: H (±1), tilt angle: γ(°), and toroidal flux: ϕ_t (Wb).

Table 3. EUHFORIA simulations, the CME models used, and the time of arrival of the CMEs at Earth in the EUHFORIA simulations.

Simulations	CME-1	CME-2	CME-3	Arrival at Earth
Run1	–	–	Spheromak	2021-11-03 21:19 UT
Run2	Spheromak	Spheromak	Spheromak	2021-11-03 20:19 UT
Observed ToA	–	–	–	2021-11-03 19:40 UT

Notes. The observed ToA (date and time in yyyy-mm-dd HH:MM format) of the CMEs from the Wind ICME catalogue are provided for comparison.

and ±10° offset in latitude and longitude around the position of Earth. There is qualitative agreement between the simulated profile and the observations, particularly concerning the arrival time. The observed passage of the shock, the sheath, and the magnetic cloud through Earth associated with this event are recorded in the Helio4cast catalogue[9] (Möstl et al. 2017). The shock reaches Earth on November 3, 2021 at 19:40 UT according to the Helio4cast catalogue. Comparing the observed arrival time to that predicted by EUHFORIA simulated Run2, we find that the shock arrives ∼39 min later at Earth as compared to the observations. If we do not take into consideration CME-1 and CME-2 in the simulations, the arrival time of CME-3 at Earth is delayed by 60 min in Run1 (with respect to observations). The early arrival of CME-3 in Run2 can be attributed to its faster expansion in the low-density region created ahead of it by the passage of CME-1+CME-2 ejecta. However, as CME-1+CME-2 only interacted with CME-3 at their flank, the arrival time difference between Run1 and Run2 is not significant (Tables 2 and 3).

The modelled number density at 1 AU is overestimated by almost an order of magnitude, as the initial density was set to 5×10^{-18} kg m^{-3} (five times the standard density as used in Scolini et al. 2019; Verbeke et al. 2019) to mitigate spheromak tilting effects in order to avoid an erroneous prediction of the magnetic field configuration (Asvestari et al. 2022). This assigned value is closer to the density value (1×10^{-17} kg m^{-3}) reported as the average observed CME density at 0.1 AU (Temmer et al. 2021). However, the observed density is derived for an extended flux rope structure, whereas a spheromak has a spherical geometry with a larger volume as compared to the flux rope geometry (see Maharana et al. 2022). Therefore, increasing the initial plasma density also increases the total mass injected into the EUHFORIA domain. Although we manage to reduce the effects of the spheromak rotation to a certain extent and reproduce the magnetic field rotations more accurately, the modelled number density at 1 AU is found to be overestimated as a trade-off.

3.5. CME magnetic field evolution

We observed the negative B_z component in the sheath before the magnetic cloud. At Earth, the minimum B_z in the sheath is enhanced by ∼44% in the presence of CME-1+CME-2 ahead of CME-3 (−6.6 nT for Run1 and −9.5 nT for Run2). The maximum B_z in the magnetic cloud of CME-3 is increased by ∼112% in the presence of the CME–CME interaction (4.2 nT for Run1 and 8.9 nT for Run2). The maximum magnetic field strength ($|B|$) is 12.5 nT for Run1 and 18.5 nT for Run2. The maximum B_z in the magnetic cloud of CME-3 is increased by ∼133% (3.9 nT for Run1 and 9.1 nT for Run2). The enhancement in the magnetic field strength in Run2 implies that the CME-1+CME-2 ejecta have an impact on the propagation of CME-3 (Fig. 9).

We analysed the 3D data by considering different planes or viewpoints. The different viewpoints are plotted in Fig. 10 to improve our understanding of the event. The discussion in this section is in reference to Fig. 11, where the scaled magnetic field strength is plotted at different stages of the evolution and interaction of the CMEs in Run2, which is shown from three different viewpoints. The magnetic field lines are colour-coded with the scaled magnetic field strength to distinguish the field lines of the magnetic cloud (stronger $|B|$) from the background solar-wind field lines. Using scaled magnetic field ($|B| \times r^2$) helps visualise the features better, which would otherwise appear fainter as magnetic field strength falls off with heliocentric distance. Time T1 corresponds to the stage when CME-1 and CME-2 started forming combined magnetic ejecta (CME-1+CME-2). At time T2, CME-3 catches up with the trailing part of CME-1+CME-2, and at time T3, CME-3 interacts through the flank of CME-1+CME-2 and takes part of the merged ejecta along in its sheath. At time T4, CME-3 has reached Earth, dragging along a small part of CME-1+CME-2 ejecta in its sheath. Viewpoint 1 (Figs. 11a-d) shows the equatorial plane ($z = 0$) and is intended to depict which parts of the CMEs impact Earth. Viewpoint 2 (Figs. 11e-h) shows a plane with its normal pointing to (0.76 AU, −0.64 AU, −0.08 AU), which is positioned along the bulk propagation direction of CME-1+CME-2 in the southward direction. Figure 11h is a zoomed-out view of the same plane. Viewpoint 3 (Figs. 11i-l) shows a plane with its normal pointing to (−0.03 AU, −0.56 AU, −0.82 AU), capturing the initial interaction of CME-3 with the flank of CME-1+CME-2 until ∼T2, after which they start drifting apart. Figure 11l is the zoomed-out view of the same plane.

Although CME-1 and CME-2 are injected 101 min apart, the faster CME-2 catches up with CME-1 and starts merging

[9] https://helioforecast.space/icmecat

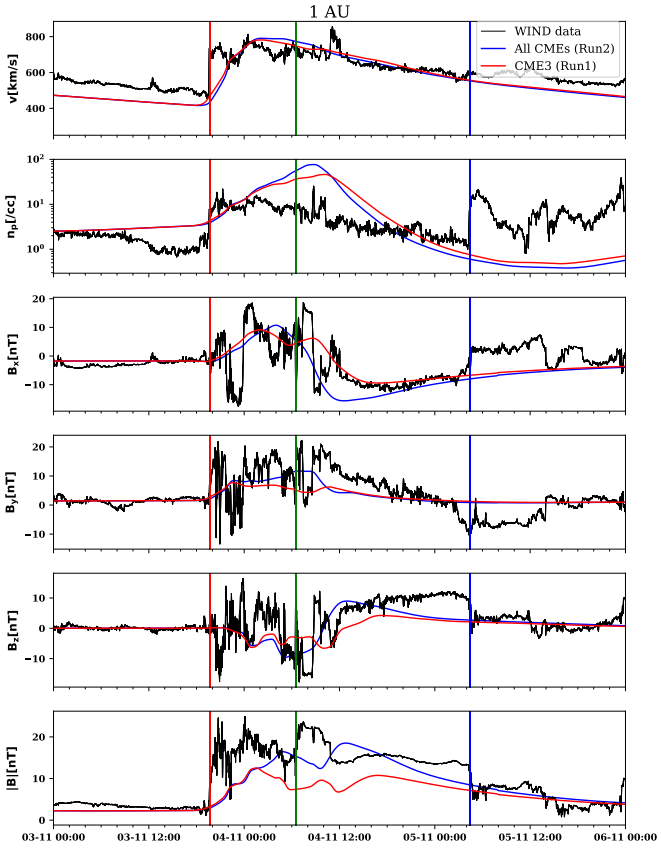

Fig. 9. Time series plot showing the comparison between simulations Run1 (only CME-3) and Run2 (CME-1, CME-2, and CME-3 modelled with the spheromak model) at Earth.

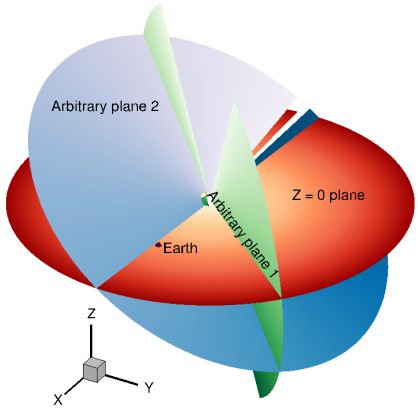

Fig. 10. Planes used for visualisation in Fig. 11: $Z = 0$ plane (red); Arbitrary plane 1 (green); and Arbitrary plane 2 (blue). The gap in the Arbitrary plane1 is because the EUHFORIA latitudinal extent ranges between ±60°.

with it within 3 h after its injection. The distance where CME-1 and CME-2 merge in the simulation is consistent with 22 $R_\odot$ as observed in the white-light observations (Sect. 2.4). The flank of the merged ejecta acts as a barrier against which CME-3 magnetic ejecta is compressed and the magnetic field strength is enhanced. The CME-1+CME-2 ejecta also experiences enhancement in magnetic field strength during the course of its propagation. There appears to be continued interaction between CME-1 and CME-2 in the combined CME-1+CME-2 ejecta as shown in Figs. 11e-h in the latitudinal extent and in Figs. 11i-l in the longitudinal extent. It is clear from these snapshots that it is the northeast flank of CME-1+CME-2 that interacts with the southwest part of CME-3 only in the initial stages of their evolution. In due course, the CMEs expand and have drifted away from each other significantly by the time of their arrival at 1 AU. The effect of the presence of CME-1+CME-2 in front of CME-3 is manifested in terms of an enhancement of the magnetic field in the CME-3 magnetic ejecta and its sheath in Run2 compared to Run1, as shown in Fig. 9b at Earth. The B_z component is more negative for Run2 compared to Run1.

In summary, with MHD modelling, we reinstate the claims made above based on the observational analysis in Sect. 2 regarding the CME–CME interaction processes, while reproducing the arrival time and magnetic field components within an acceptable margin of error. The size of the sheath region is not well reproduced in the simulations. The reason for this can be attributed to the use of the spheromak CME model and the injection only at 0.1 AU. As the model has a spherical geometry lacking the legs of the CME structure, the flank encounters are poorly modelled (Maharana et al. 2022). Moreover, the sheath forms in the lower solar corona, while in the simulation the spheromak model (without a sheath) is injected only at 0.1 AU and the sheath can start forming only then. This is a known defect of the simplified model. The extent of the impact due to CME-1 and CME-2 may be underestimated given the lack of their global geometry. Therefore, the part of the CME-1+CME-2 ejecta that CME-3 dragged along during its heliospheric propagation may also be underestimated, which means the sheath may be wider than predicted here. In addition, EUHFORIA simulations are currently limited in terms of modelling the sheath region as the MHD formulation on its own lags behind in mimicking the micro-scale processes that enhance magnetic reconnection forming a sheath.

4. Prediction of geo-effectiveness and interaction effect at 1 AU

In this section, we analyse the possible changes to the geo-effectiveness due to the CME–CME interaction using a prediction of the geomagnetic disturbances as indicated by the SYM-H index (which can be considered as a high-resolution Dst index). The prediction uses data from the solar wind at 1 AU as input and obtains the expected response of the ring current as observed on the ground by the SYM-H index. We carried out the analysis by creating three predictions, each of them from a different set of input data from the solar wind. The first prediction uses the observed solar-wind data, the second uses the solar wind as modelled in Run1, thus considering only CME-3, and the last one uses the solar wind as modelled by Run2, thus considering the three CMEs.

4.1. Data input

The data input used and the results are given in Fig. 9. Black solid lines represent observed parameters, which for the first three panels (v, bulk solar-wind speed in the radial direction; B_z, the vertical component of the IMF; and n, the solar-wind proton density) are the solar-wind data. The same line in the last panel is the observed SYM-H index. These data are obtained from the high-resolution data in OMNIweb (HRO) (King & Papitashvili 2005).

Red and blue solid lines belong to the Run1 (only CME-3) and Run2 (all CMEs) respectively Fig. 12, on the first and second

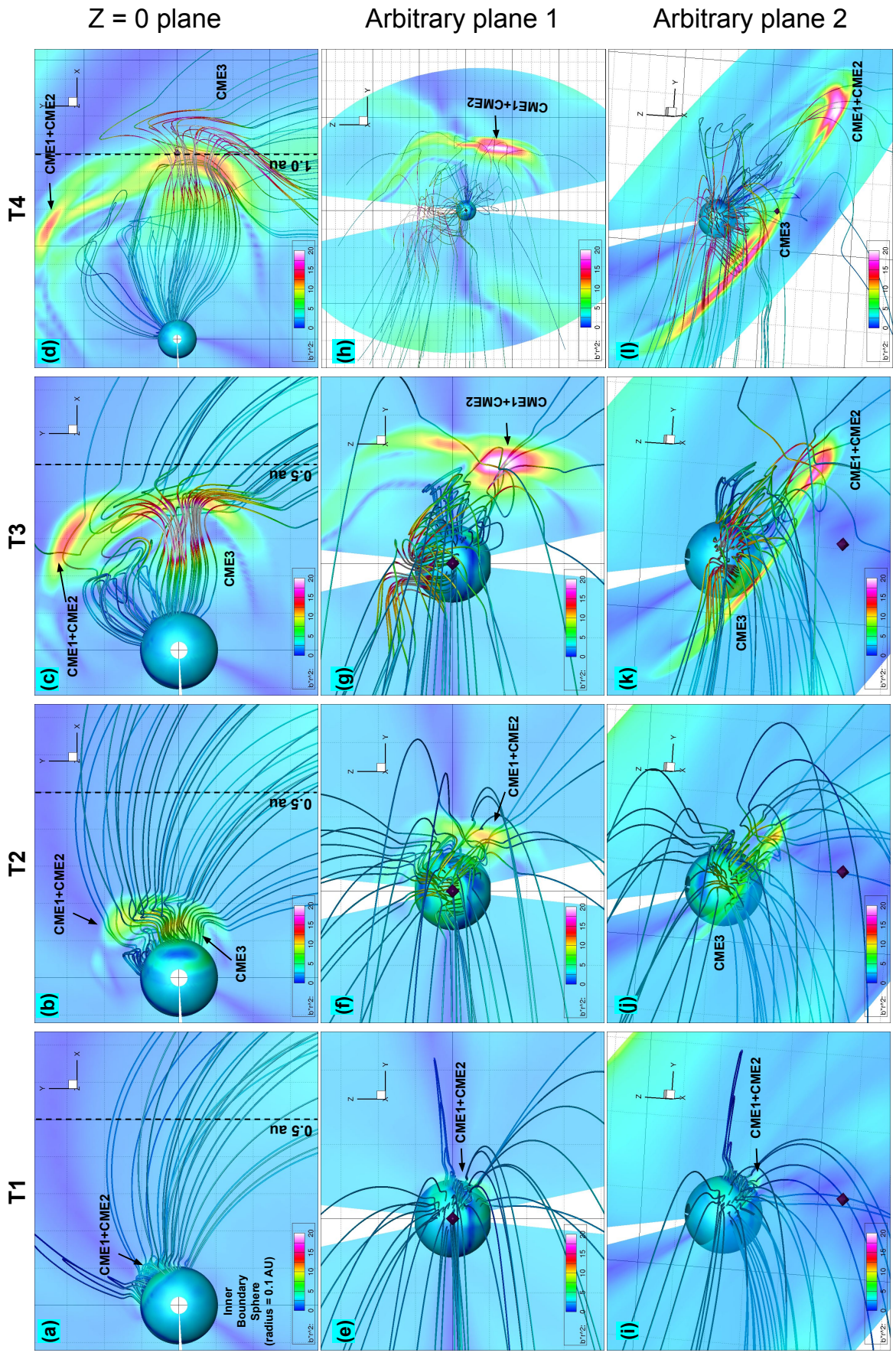

T1: 2021-11-02 03:59 →CME1+CME2
T2: 2021-11-02 09:59 →CME3 interaction with trailing part of CME1+CME2
T3: 2021-11-02 20:59 →CME3 further pushes through the flank of CME1+CME2
T4: 2021-11-04 03:59 →Arrival of the CME3 shock at 1 au

Z = 0 plane : Equatorial plane (XY)
Arbitrary plane 1: With its normal pointing to (0.76 AU, -0.64 AU,-0.08 AU)
This plane is drawn to visualise the latitudinal extent of CME1+CME2 going south of the ecliptic.
Arbitrary plane 2: With its normal pointing to (-0.03 AU, -0.56 AU,-0.82 AU)
This is a mutual plane to capture the latitudinal extent of both CME1+CME2 and CME3.

Fig. 11. Temporal evolution of the CMEs from a different viewpoint (a-d) $Z = 0$ (equatorial plane); (e-h) Arbitrary plane 1; and (i-l) Arbitrary plane 2.

plots for the solar-wind data and on the last plot for the predictions obtained from the respective solar-wind data from the simulations. The orange solid line in the last panel is the prediction from the observed solar-wind data (black solid lines on the first and second panels).

4.2. Prediction method

The predictions are computed using the well-known empirical relationship given by Burton et al. (1975). This relationship is given as the linear response of a system to a given injection function. Consequently, two definitions are needed, one for the response of the system and another for the injection function.

The system is defined as a first-order linear time-invariant system with a fixed characteristic time constant (τ) modelled by the following differential equation:

$$\frac{\mathrm{d}}{\mathrm{d}t}\mathrm{SYM} - \mathrm{H}_0 = F(E) - \frac{1}{\tau}\mathrm{SYM} - \mathrm{H}_0. \quad (1)$$

The original formulation given in Burton et al. (1975) yields a value of $\tau = 7.716$ h.

The injection function $F(E)$ is given by the dawn-to-dusk convective electric field ($E_y = VB_z$; where V represents the solar-wind speed and B_z stands for the IMF south component in GSM coordinates) as follows:

$$F(E) = \begin{cases} 0: & E_y < 0.50 \quad \mathrm{mV/m}, \\ \mathrm{d}(E_y - 0.5): & E_y > 0.50 \quad \mathrm{mV/m}, \end{cases}$$

where $d = -10^{-3}$ nT m/(s mV).

Using Eq. (1), we obtain SYM-H_0 as the convolution of the first-order impulse response and the $F(E)$ signal on the input. SYM-H_0 is a prediction of the effects of the ring current enhancement on the horizontal geomagnetic field component due to solar-wind energy input; consequently, the prediction would need to be delayed to take into account the propagation time from the solar-wind measurement position to the ground, but this is not necessary in the case presented here because solar-wind data from OMNIWeb are already shifted to the bow-shock (King & Papitashvili 2005).

Furthermore, it is necessary to add the effect of the change of solar-wind dynamic pressure and to subtract a 'quiet day' constant, as indicated by Eq. (2):

$$SYM\text{-}H = SYM\text{-}H_0 + b(P_d)^{1/2} - c, \quad (2)$$

where $b = 0.2\,\mathrm{nT(eV\,cm^{-3})^{-1/2}}$, $c = 20$ nT, and $P_d = N_\mathrm{p}\,V^2\,10^{-2}$ eV cm^{-3}, with N_p being the solar-wind proton density. The resultant SYM-H index includes the prediction plus the effect of the solar-wind dynamic pressure. In order to better characterise the prediction, we added the same effect from the dynamic pressure to all three predictions. This means that we calculated the dynamic pressure following Eq. (2) using the observed solar-wind density and speed, and add the same result to each of the predicted SYM-H.

4.3. Geo-effectiveness

The results of each of the predictions are plotted in the bottom panel of Fig. 12. The predicted SYM-H (−125 nT) index from observed solar-wind data (orange solid line) is comparable in all major features of the observed SYM-H. The predicted sudden storm commencement (SSC) at the beginning of the event is not as pronounced as it is in the observations, but the other features, even the double peak at the end of the main phase of the storm, are reproduced quite well. This means that the geo-effectiveness of the event is well represented when taking into account only the speed (v) and the (B_z) component of the IMF as proposed by this empirical model. The predictions from the simulated solar-wind data (blue and red solid lines, representing all CMEs and only CME-3, respectively) do not follow the observed SYM-H as closely as the above model, but they reproduce the main phase feature of the geomagnetic storm; however, we note that both predict a storm of lower intensity than that seen in the observations. The main differences between the two predictions (from simulated solar wind) are the intensity of the storm (peak of SYM-H) and the time at which it occurs. In this instance, the prediction (SYM-H = −98 nT) from all CMEs approaches the observed value, particularly during the initial peak. The observed second dip (black line) is not represented by the prediction with all CMEs accounted for. In the case of the prediction with only CME-3, the intensity of the predicted storm is only about −67 nT, which is half of the observed values. The analysis based on our modelling results suggests an enhancement of the geo-effectiveness of the storm due to the interaction between the CMEs of a factor of ∼1.5. We come to this conclusion based on the comparison of the minimum Dst computed using the modelling results from Run1 and Run2.

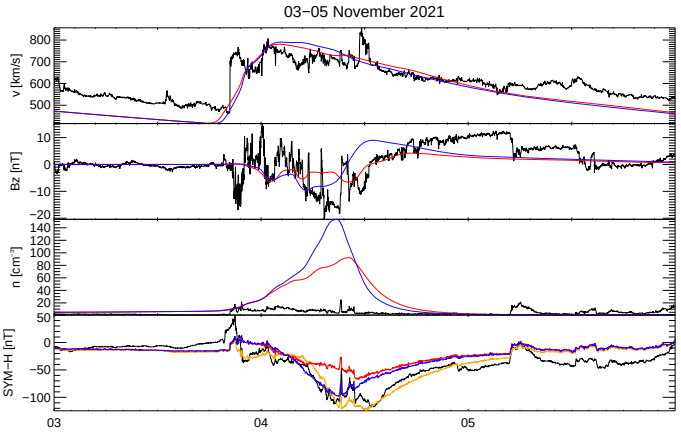

Fig. 12. Prediction of SYM-H (bottom panel) indicating the geo-effectiveness expected from different simulations (all CMEs = blue, only CME 3 = red) compared to the expected SYM-H from the input given by the observed parameters in the solar wind (orange).

From these results, we can see an increase in the geo-effectiveness from the interaction of the CMEs (blue line) when compared to the geo-effectiveness of only one CME (red line). Comparing the intensity of the prediction from the observed solar wind with the prediction that includes all CMEs, we can also conclude that the geo-effectiveness of the event is considerably enhanced when all CMEs are accounted for and that the observed SYM-H is probably the result of the interaction of the CMEs, even though the second peak in the main phase is not properly reproduced by the prediction (expected geo-effectiveness from the simulation with all three CMEs).

5. Discussion and conclusions

One of the most significant eruptive activities in solar cycle 25 occurred on November 1-2, 2021, with a barrage of M 1.6-class eruptive flares in rapid succession accompanied by several CMEs. We used observations of these CMEs from multiple viewpoints to reconstruct their 3D geometry and kinematics,

and to identify their interaction and geo-effectiveness. We investigated a diverse set of three CMEs and their varied interactions detected concurrently at heights from the upper corona to 1 AU from several viewpoints. We used the GCS model to estimate the source, trajectory, geometry, and kinematics of these CMEs before their contacts from two coronagraphic perspectives (COR2: STEREO-A and C2/C3: LASCO/SOHO). We then ran 3D MHD EUHFORIA simulations to understand the interaction heights and characteristics. According to our analysis, CME-1 is a slow-rising gradual event that originated north of the Sun–Earth line. CME-2 is a moderately impulsive event associated with a C-class soft X-ray flare. CME-2 is 47° in width and has an initial constant velocity of 829 km s^{-1}. CME-3 is a huge impulsive event with an M 1.6 class X-ray flare, a constant velocity of 1335 km s^{-1}, and produces a shock that has a wide influence on the corona and is visible as a halo from all angles. CME-1 and CME-2 interactions with CME-3 are likewise very diverse. In summary, we performed 3D reconstructions of the three CMEs simultaneously. Individual CME outlines are difficult to distinguish from one specific viewpoint and necessitate simultaneous examination of all available data from all possible angles. We further confirm that the fits for a number of image-processing methods, such as running difference, base difference, and background removal, are compatible with the reported white-light signatures and overall coronal morphology. Finally, we are confident that we can distinguish and fit all three structures to achieve very consistent kinematic results. The direction and width of a CME are essential parameters in determining a correct estimation of its arrival time and the amplitude of the ICME structure. Further, we simulated the heliospheric propogation of all three reported CME events (discussed in Sect. 3.3) using EUHFORIA. We modelled each event as a flux-rope structure using a linear force-free spheromak CME model, which allows a more realistic propagation and evolution analysis of CMEs in the heliosphere. The comparison of EUHFORIA results of the solar-wind properties at 1 AU enables us to relate the ICME characteristics measured by in situ spacecraft. We observed that, in the presence of CME-1+CME-2 ahead of CME-3, the minimum Bz in the sheath at Earth is increased by approximately ∼44% (−6.6 nT for Run1 and 9.5 nT for Run2). In the presence of the CME–CME interaction, the highest Bz in the magnetic cloud of CME-3 increases by ∼112% (4.2 nT for Run1 and 8.9 nT for Run2). The maximum magnetic field strength is 12.5 nT for Run1 and 18.5 nT for Run2, respectively. We analysed the effects of the CME–CME interaction on geo-effectiveness using an empirical relationship given by Burton et al. (1975). The prediction provides the expected response of the ring current as measured by the SYM-H index from data obtained from the solar wind at 1 AU. Three forecasts are made as part of the study, each based on a different set of solar-wind input data. The first one uses data for the observed solar wind, the second uses the solar wind as modelled in Run1, using only CME-3, and the third uses the solar wind as modelled in Run2, taking all three CMEs into account.

Several intriguing conclusions emerge from our analysis of the observed CME–CME interaction event:

1. CME-1 is accelerated to the same speed as CME-2 after interaction. At the 22 $R_\odot$ height, CME-1 and CME-2 merged fully and became indistinguishable, we can clearly detect the cannibalism by CME-2 on CME-1 from observations (Sect. 2.4).
2. CME-3 loses energy and slows down as it propagates to the Sun–Earth line. According to observations made from the white-light running-difference images, the CME event that occurred on 2 May 2013 05:24 UT interacts with two CMEs at the heliocentric distance around 45 $R_\odot$ (Sect. 2.4).
3. Our EUHFORIA MHD simulation (Run2) corroborates the white-light observations, confirming that CME-1 and CME-2 merge at ∼22 $R_\odot$. Subsequently, the flank of CME-3 interacts with the flank of merged CME-1 and CME-2 ejecta at the height of ∼45 $R_\odot$ in the simulation domain (Sect. 3.3).
4. Comparing the observed arrival time to that predicted by the EUHFORIA simulation Run2, we find that the shock reaches Earth ∼39 min later than predicted. If CME-1 and CME-2 are not included in the simulations, the arrival time of CME-3 to Earth is delayed by ∼60 min in Run1 (in comparison to observations). CME-3 arrives early in Run2 due to its rapid expansion in the low-density region formed ahead of it by the passage of CME-1+CME-2 ejecta. The arrival-time discrepancy between Run1 and Run2 is not substantial because CME-1+CME-2 only collided with CME-3 at their flanks (Sect. 3.5).
5. The in-situ observations suggest potential indications of CME-3, implying that the passage of the shock might have caused an increase in temperature within the CME plasma. In addition, the comparable long duration of the sheath region and the significant variation in the southward component of the interplanetary magnetic field starting within the sheath yield the interaction of the flank of merged CME-1+CME-2 structure with following CME-3. Which further observed and confirmed by EUHFORIA simulations of enhanced Bz in the magnetic cloud of CME-3 by ∼133% (3.9 nT for Run1 and 9.1 nT for Run2) (Sect. 3.5).
6. In situ observations at 1 AU suggest that the geomagnetic storm is generated by the sheath. Our comparison of simulation results suggests an enhancement of the geo-effectiveness of the storm due to the interaction between the CMEs of a factor of ∼1.5. Additionally, based on simulations and their comparison to observations, we conclude that the evolution of the reported interactive CMEs doubled their geo-effectiveness. The geo-effectiveness of all three CMEs increased significantly – that is, by a factor of 2 – compared to the geo-effectiveness of CME-3 alone, and therefore the observed SYM-H is likely the consequence of the interaction of the CMEs (Sect. 4).

The propagation characteristics of CME interactions may have substantial ramifications for space weather forecasts, such as large changes in trajectory and velocity. We can anticipate and describe the effect at Earth of these CMEs using both the Earth (L1-point) and STEREO views. Our findings reveal that CME–CME interactions are susceptible to the 3D position of the magnetic structures of the CMEs relative to each other. An off-axis observation is required to correctly see and anticipate the effects of these discrepancies in CME–CME interactions at Earth (Vourlidas et al. 2017). Furthermore, the CMEs studied here interacted near the Sun, highlighting the need for comprehensive coverage of observations from the solar surface to Earth from numerous perspectives.

We hypothesise that CME–CME interactions contribute to their geo-effectiveness, as higher temperatures are observed in the structure following the shock. In the scenario studied here, this effect could be attributed to CME-3 itself and the super radial expansion of the flux-rope. We also observe an unusual small-scale structure within the sheath region, which could play a major role in the enhancement of geo-effectiveness. We hope to explore these factors; however, this would

Table 4. Required instruments with desired observations, resolution, and location of spacecraft to investigate the characteristics and geo-effectiveness of CME–CME interactions.

Science Traceability Matrix				
Objective: To investigate the CME–CME interaction region from L1				
Science topics	Instruments	Measurement requirements	Spacecraft requirements	SWIFT
Source region identification	Magnetogram, EUV, visible imager	EUV imager and magnetograph to obtain full-disc images with 1″ pixels; 1 min cadence; WL coronagraph (15″ pixels; FOV 1−30 Rs)		SWIFT will provide continuous observations from L1 and sub-L1
Spatial characteristics	Field suite, Plasma suite	<1 s resolution	Orbits: Halo orbits at L1;	Locations with <1 s
Temporal evolution properties	Field suite, Plasma suite	<1 s resolution	No. of Probes: At-least 2 (or more)	Resolution for Mag, plasma, and particle
Particle energisation	Particle detector	Energy ranges: 10 eV to 25 keV, Mass Resolution: 0.5 to >1 amu for H^+, He^+ and Heavy ions	with ~50−200 Re separation	Observations with ~150 Re separation
Geo-effectiveness	Ground-based magnetometers	<1 s resolution		(radial and longitudinal)

necessitate a more extensive examination of the in situ data and MHD simulation, which is beyond the scope of the present study.

A comprehensive understanding of the complex structure and evolution of such ICME formations is of significant importance in ensuring improved predictions of their geo-effectiveness. Table 4 provides our proposed list of requirements to investigate the CME–CME interaction characteristics at 1 AU. To this end, the Space Weather Investigation Frontier (SWIFT; Akhavan-Tafti et al. 2023) is designed to investigate the three-dimensional temporal and spatial evolution dynamics of ICMEs at small and meso-scales using a multitude of spacecraft from the vantage point of sub-L1.

Acknowledgements. The authors recognize NASA's open data policy for SOHO, STEREO, SDO, ACE and WIND data. This work is supported by the National Aeronautics and Space Administration (NASA) under Grant No. 80NSSC23K0674 issued through the Heliophysics Flight Opportunities Studies (HFOS) program under the Research Opportunities in Space and Earth Sciences (ROSES 2022).This paper uses data from the CACtus CME catalog, generated and maintained by the SIDC at the Royal Observatory of Belgium. We thank of Johan N., for python codes for GCS model Johan (2021) and his suggestions. The code for GCS modeling in Python is available at https://github.com/johan12345/gcs_python (https://doi.org/10.5281/zenodo.5084818). S.P. and A.M. acknowledge support from the projects C14/19/089 (C1 project Internal Funds KU Leuven), G.0B58.23N and G.0025.23N (FWO-Vlaanderen), SIDC Data Exploitation (ESA Prodex-12), and Belspo project B2/191/P1/SWiM.

References

Akhavan-Tafti, M., Johnson, L., Sood, R., et al. 2023, Front. Astron. Space Sci., 10, https://doi.org/10.3389/fspas.2023.1185603
Asvestari, E., Rindlisbacher, T., Pomoell, J., & Kilpua, E. K. J. 2022, ApJ, 926, 87
Brueckner, G. E., Howard, R. A., Koomen, M. J., et al. 1995, Sol. Phys., 162, 357
Burton, R. K., McPherron, R., & Russell, C. 1975, J. Geophys. Res., 80, 4204
Chandrasekhar, S., & Woltjer, L. 1958, Proc. Nat. Acad. Sci., 44, 285
Dissauer, K., Veronig, A. M., Temmer, M., Podladchikova, T., & Vanninathan, K. 2018, ApJ, 855, 137
Domingo, V., Fleck, B., & Poland, A. 1995, Space Sci. Rev., 72, 81
Farrugia, C. J., Jordanova, V. K., Thomsen, M. F., et al. 2006, J. Geophys. Res., 111, 11104
Gopalswamy, N., Yashiro, S., Kaiser, M. L., Howard, R. A., & Bougeret, J.-L. 2001, ApJ, 548, L91
Harrison, R. A., Davies, J. A., Möstl, C., et al. 2012, ApJ, 750, 45
Howard, R. A., Moses, J., Vourlidas, A., et al. 2008, Space Sci. Rev., 136, 67
Johan, L. 2021, https://github.com/johan12345/gcs_python
Joshi, B., Ibrahim, M. S., Shanmugaraju, A., & Chakrabarty, D. 2018, Sol. Phys., 293, 107
Kaiser, M. L., Kucera, T. A., Davila, J. M., et al. 2008, Space. Sci. Rev., 136, 5
Kazachenko, M. D., Lynch, B. J., Welsch, B. T., & Sun, X. 2017, ApJ, 845, 49
King, J., & Papitashvili, N. 2005, J. Geophys. Res.: Space Phys., 110, A2
Koehn, G., Desai, R., Davies, E., et al. 2022, ApJ, 941, 139
Lemen, J. R., Akin, D. J., Boerner, P. F., et al. 2011, The Solar Dynamics Observatory (Springer), 17
Liu, Y. D., Luhmann, J. G., Möstl, C., et al. 2012, ApJ, 746, L15
Lugaz, N., & Farrugia, C. J. 2014, Geophys. Res. Lett., 41, 769
Lugaz, N., Manchester, W. B., IV, & Gombosi, T. I. 2005, ApJ, 634, 651
Lugaz, N., Farrugia, C. J., Manchester, W. B., IV, & Schwadron, N. 2013, ApJ, 778, 20
Maharana, A., Isavnin, A., Scolini, C., et al. 2022, Adv. Space Res., 70, 1641
Maharana, A., Scolini, C., Schmieder, B., & Poedts, S. 2023, A&A, 675, A136
Mishra, W., & Srivastava, N. 2014, ApJ, 794, 64
Mishra, W., Srivastava, N., & Davies, J. A. 2014, ApJ, 784, 135
Mishra, W., Srivastava, N., & Singh, T. 2015, J. Geophys. Res. (Space Phys.), 120, 10
Mishra, W., Wang, Y., & Srivastava, N. 2016, ApJ, 831, 99
Mishra, W., Wang, Y., Srivastava, N., & Shen, C. 2017, ApJS, 232, 5
Möstl, C., Farrugia, C. J., Kilpua, E. K. J., et al. 2012, ApJ, 758, 10
Möstl, C., Isavnin, A., Boakes, P. D., et al. 2017, Space Weather, 15, 955
Palmerio, E., Nieves-Chinchilla, T., Kilpua, E. K., et al. 2021, J. Geophys. Res.: Space Phys., 126, e2021JA029770
Pomoell, J., & Poedts, S. 2018, J. Space Weather Space Clim., 8, A35
Scolini, C., Rodriguez, L., Mierla, M., Pomoell, J., & Poedts, S. 2019, A&A, 626, A122
Scolini, C., Chané, E., Temmer, M., et al. 2020, ApJS, 247, 21
Sheeley, Jr., N. R. 2017, Hist. Geo- Space Sci., 8, 21
Shen, C., Wang, Y., Wang, S., et al. 2012, Nature, 8, 923
Temmer, M., Veronig, A. M., Peinhart, V., & Vršnak, B. 2014, ApJ, 785, 85
Temmer, M., Holzknecht, L., Dumbović, M., et al. 2021, J. Geophys. Res. (Space Phys.), 126, e28380
Thernisien, A. 2011, ApJS, 194, 33
Tschernitz, J., Veronig, A. M., Thalmann, J. K., Hinterreiter, J., & Pötzi, W. 2018, ApJ, 853, 41
Verbeke, C., Pomoell, J., & Poedts, S. 2019, A&A, 627, A111
Vourlidas, A., Balmaceda, L. A., Stenborg, G., & Lago, A. D. 2017, ApJ, 838, 141
Yashiro, S., Gopalswamy, N., Michalek, G., et al. 2004, J. Geophys. Res.: Space Phys., 109, A7